applied sciences

MDPI

Article

Composite Forming Technology for Braiding Grid-Enhanced Structures and Design of a New Weaving Mechanism

Jiakai Wei [1] and Wuxiang Zhang [1,2,*]

[1] School of Mechanical Engineering and Automation, Beihang University, Beijing 100191, China; by1707111@buaa.edu.cn
[2] Ningbo Institute of Technology, Beihang University, Ningbo 315832, China
* Correspondence: zhangwuxiang@buaa.edu.cn

Abstract: Three-dimensional weaving structures have high strength and resistance to interlayer shear due to their integrated manufacturing features. The traditional weaving equipment is generally huge and is not effective for weaving small-sized products. Therefore, this paper proposes a new composite forming technology and weaving mechanism based on grid-enhanced structures to braid small-sized preforms, combining the continuous fiber printing technology, the rope drive technology and the 3D weaving technology. This paper adopted the screw theory for forward and inverse kinematic analysis of the weaving mechanism and applied software Adams2020 for trajectory simulation analysis. The theoretical calculation results were basically consistent with the simulation results, which verified the rationality and feasibility of the designed weaving mechanism in small, enhanced grids.

Keywords: composite forming method; grid-enhanced structures; weaving mechanism; rope drive mechanism; kinematic

check for updates

Citation: Wei, J.; Zhang, W. Composite Forming Technology for Braiding Grid-Enhanced Structures and Design of a New Weaving Mechanism. *Appl. Sci.* **2023**, *13*, 11788. https://doi.org/10.3390/app132111788

Academic Editor: Kang Su Kim

Received: 12 September 2023
Revised: 22 October 2023
Accepted: 27 October 2023
Published: 27 October 2023

Copyright: © 2023 by the authors. Licensee MDPI, Basel, Switzerland. This article is an open access article distributed under the terms and conditions of the Creative Commons Attribution (CC BY) license (https://creativecommons.org/licenses/by/4.0/).

1. Introduction

Composite material preforms fabricated through the three-dimensional weaving technology contain fibers oriented in multiple directions and distributed in three-dimensional space. This structure has the advantage of preventing or retarding the propagation of interlayer cracks in the composite material under impact load, significantly improving the lateral performance of the composite material [1–3]. Therefore, the impact damage tolerance and fracture toughness of three-dimensional weaving composite materials are extremely higher than those of laminated plates [4,5]. Three-dimensional woven composite materials are suitable for weaving various complex geometric shapes that can be realized by using different weaving methods and varying weaving angles, yarn density and other parameters, without extensive mechanical processing [6]. Currently, depending on the weaving technique they use, weaving machines are mainly divided into two categories: Cartesian weaving machines and three-dimensional rotary weaving machines. Cartesian weaving machines mainly perform two-step weaving, four-step weaving and multiple-step weaving. The woven yarns in the fabric under production run in the thickness direction and are interwoven between layers to form an internal lock between adjacent layers [7]. Benefiting from the braiding technology the use, rotary weaving machines can operate at a higher braiding speed. However, the cross-sectional shapes of the prefabricated components that they produce are mostly circular, quadrilateral, I-shaped and branched. In addition, defects are visible in the structure of variable-cross section 3D woven fabrics and branched fabrics for medical therapy such as artificial coronary arteries and blood vessels [8,9]. At the same time, these weaving methods required huge equipment, long production cycles, a complex forming technology, and high expenses, which are merely convenient in special situations [10–13].

Traditional weaving techniques are inapplicable to weave small-sized structures. The catheter interventional technology applied in the therapy of blood vessel diseases has

the advantages of reliability, minimal invasion and safety. It was inspired by the three-dimensional weaving method for small-sized structures. In the rope drive technology, the motor and other drive units are placed externally, which greatly reduces the mass and volume of the system terminal and provides high operation flexibility and strong load capacity. In addition, the external drives can effectively reduce the vibrations of system terminal, greatly improving its operating accuracy [14–16]. Y. Haga and Y. Tanahashi developed an active catheter with a diameter of 1.2 mm [17]. Y. Hagal prepared a titanium–nickel super-elastic alloy (SEA) catheter through laser micromachining. The catheter consisted of titanium–nickel super-elastic alloy (SEA) tubing and silicone rubber tubing, with the silicone rubber tubing covering the outside of the SEA tubing. The outer diameter of the prefabricated, curved active catheter was 0.94 mm, and the inner diameter was 0.85 mm [18]. J.K. Chang et al. developed an active catheter bending guidance robot system with an outer diameter of 3.0 mm, an inner diameter of 2.0 mm, and a length of 1000 mm [19]. William W. Cimino, from the Department of Bioengineering at the University of Utah, developed an active catheter tip for cardiac treatment based on the advantages of rope drive and studied corresponding active control technologies. The diameter of the conduit shell was 1 mm, the rope was stainless-steel wire with a diameter of 0.1 mm, and the conduit material was polytetrafluoroethylene (PTFE) [20].

Since the traditional weaving equipment is generally huge and not suitable for weaving small-sized products, this study adopted a catheter interventional technology to innovatively design a weaving mechanism suitable for braiding in a small space. In addition, this paper proposes a new weaving process applicable to the weaving mechanism, which mainly consists of the continuous fiber printing technology to print grid-enhanced structures for supporting the subsequent weaving. This article is organized as follows: Section 2 specifically presents the weaving process principle applied for printing the grid structure, the weaving technology and the injection methods, which combined the technology of continuous fiber printing, the catheter interventional technology and the 3D weaving technology; Section 3 specifically describes the 3D model of weaving system, i.e., its size, composition and function. The weaving process, including step sequence and weaving steps, is presented; Section 4 analyzes the forward and inverse kinematics of the rope-drive mechanism based on screw theory and draws the operating space; Section 5 reports the calculation of the rotation angle of each joint and the introduction of the calculated results into forward kinematics to prove the rationality and correctness of the weaving mechanism. In addition, the dynamic simulation analysis of the weaving mechanism was conducted through Adams software. The simulated trajectories furtherly verified the accuracy of the forward and inverse solutions calculated through screw theory and indicated the rationality and feasibility of the designed weaving mechanism in small enhanced grids.

2. Weaving Process Principle

Currently, due to the softness of the weaving fibers, it is usually necessary to prepare support structures in advance for the three-dimensional weaving of complexly shaped products. Therefore, in order to weave the desired product, this study combined the continuous fiber printing technology and the 3D pure-substrate printing technology to print grid-enhanced structures, which provided the required supporting structure for subsequent weaving. The design of a grid structure mainly depends on the size and stress conditions of the target fabric structure and on the accuracy of the weaving mechanism, which has to allow the fabrication of personalized weaving products. The enhanced grid unit applied in this article was a cube with length, width and height of 4 mm. The specific process steps were as follows. First, we applied the hierarchical design method to design the corresponding grid structure shown in Figure 1d (including the number of layers and the shape of the grid element) based on the shape and size of the fabric. The grid element could be a regular polyhedron, a cylinder, or a combination of various polyhedrons, which facilitated weaving with curved structures. Secondly, using the continuous fiber-reinforced 3D technology for layered printing shown in Figure 1b, the reinforced fibers are mainly

distributed in XY direction, the support between layers is printed without reinforced fibers, as shown in Figure 1a,c. Thirdly, we used the designed weaving machine to weave within the grid unit, as shown in Figure 1e. Fourth, we performed layered printing and weaving, as shown in Figure 1f, forming a cross-linked, locked inner structure, as shown in Figure 1h. The distribution of the woven fibers depends on the structural stress and other factors, as long as they act on the Z direction of the reinforcement. Last, we used appropriate matrix materials to inject and fill the three-dimensional woven fabric, obtaining the final three-dimensional woven entity shown in Figure 1g.

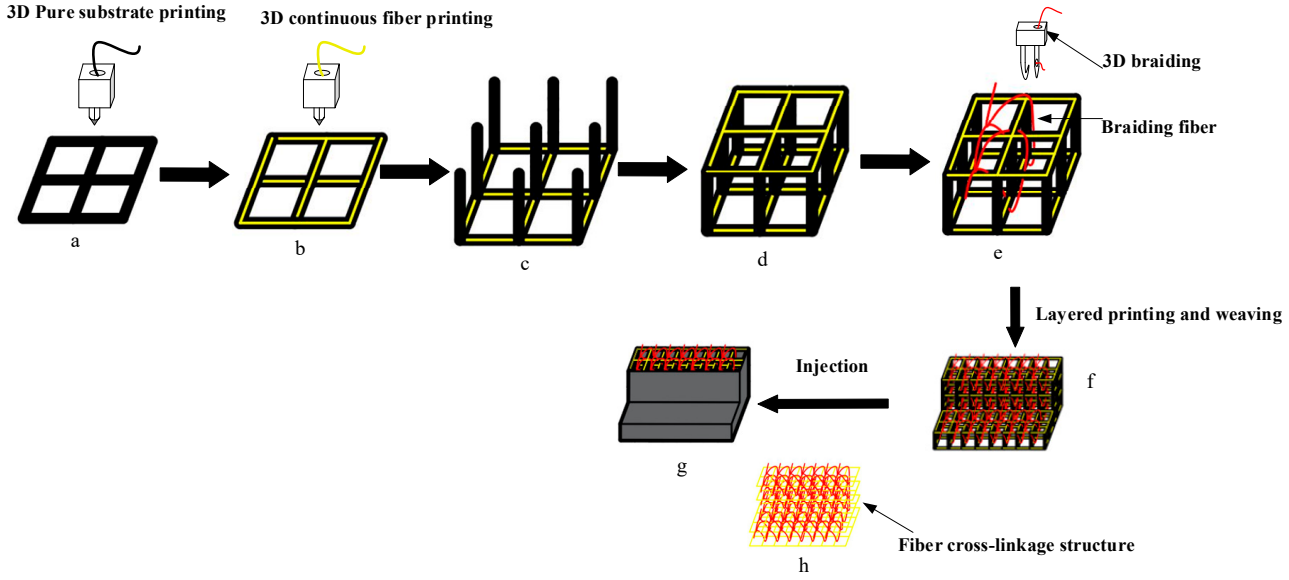


Figure 1. The weaving process principle. (**a**) the layer printed without reinforced fibers; (**b**) the layer strengthened by fibers; (**c**)the support between layers; (**d**) the grid-enhanced structure; (**e**) 3D braiding in grid-enhanced structure; (**f**) woven structure; (**g**) injection mold; (**h**) fiber cross-linkage structure.

3. Design of the 3D Weaving Mechanism and Weaving Process

3.1. Design of the 3D Weaving Mechanism

To complete fiber weaving between different small-sized grids, a 3D weaving mechanism had to be designed, particularly to introduce the fibers in a small space. As shown in Figure 2, the 3D weaving mechanism mainly consists of a rope drive, a thread picking device and a hook unit. Inspired by the characteristics of soft robots that can move in narrow spaces, the rope drive was designed to transfer the weaving fibers from the interior of one grid to the interior of another grid, which would facilitate the hooking work of crochet needles. The rope drive shown in Figure 2c consists of a winding shaft, a tensioner pulley, a coupling system, an electric motor pulley, which has the significant function of transferring the weaving fibers to the hook through small spaces. The mechanism has four rotational joints to ensure the transfer of the fibers in the grid structures during the weaving process. Due to the fact that the rope can only be pulled but not compressed, the driving control of the rope drive active conduit is different from that of conventional robotic arms. Thence, we adopted eight motors to control the joints and achieve force closure, and each two motors were responsible for the rotation of one joint. The diameter of the winding shaft shown in Figure 2d was 5 mm; high-precision rope length drive control was achieved by adopting the appropriate stepping motor. The accuracy of the rope drive mechanism could reach about 0.06 mm.

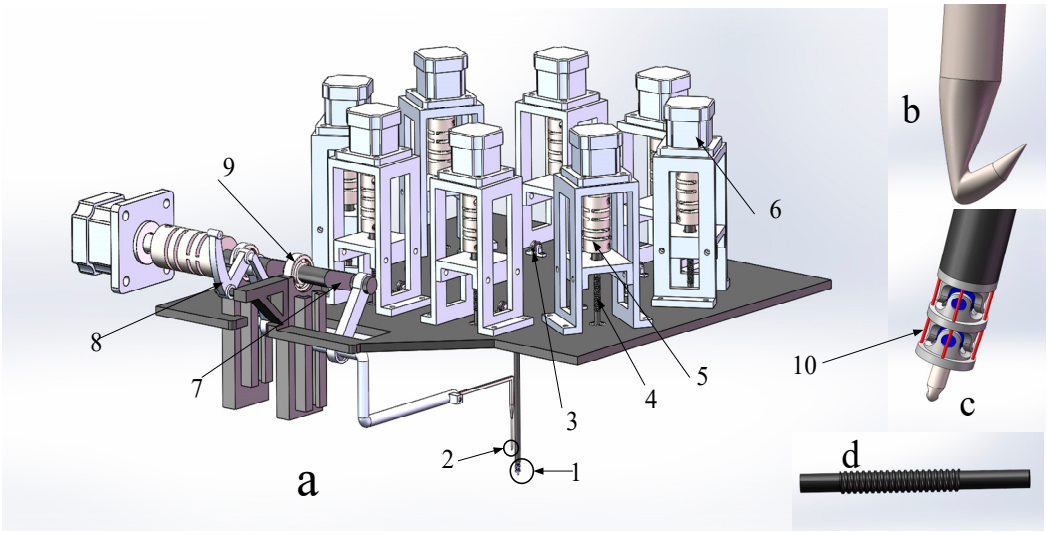


Figure 2. (**a**) The weaving mechanism (1, end of the rope drive; 2, crochet hook; 3, tensioner pulley; 4, winding shaft; 5, coupling system; 6, electric motor pulley; 7, crank–slider mechanism; 8, thread picking device; 9, rolling bearing; 10, driven rope); (**b**) partial enlarged drawing of the crochet hook; (**c**) partial enlarged drawing of the rope drive; (**d**) partial enlarged drawing of the winding shaft.

This study adopted a crank–slider mechanism to control the hook and the thread picking device, which facilitated the control of the system and simplified its structure. The crank–slider mechanism mainly contained a crochet, a thread picking device, crank–slider and rolling bearings. As shown in Figure 3, the length of crank R_1 was 15 mm, and the length of the connecting rod L_1 was 25 mm; meanwhile, R_2 was 10 mm long, and L_2 was 25 mm long. The length of the connecting rod L_3 was 35 mm. The rod of the thread picking device, L_4, was 15 mm long, while L_5 was 22 mm long, and the intersection angle θ between them was 60°. The length of L_6 was 31 mm. To satisfy the time requirements of the braiding process, the thread picking device released the weaving fiber as the hook picked up the thread loop and tightened the weaving fiber as the hook picked it up. The phase difference between the hook and thread picking operations was designed to be 180°. The terminal position of the crochet relative to the coordinate system $x_0y_0z_0$ of the rope drive was set to be $\begin{bmatrix}1.6\text{ mm} & 1.2\text{ mm} & -1.6\text{ mm}\end{bmatrix}^T$. The crochet's connecting rod was designed to be bent, as shown in Figure 2, to prevent interference between the rope drive and the hook during the weaving process.

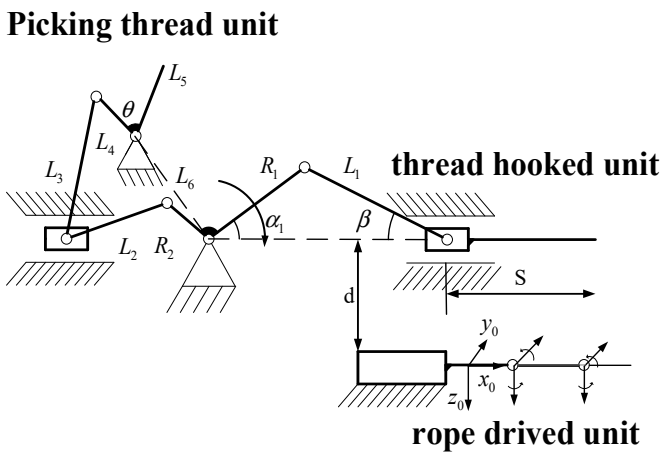


Figure 3. The schematic diagram of the weaving mechanism.

3.2. Design of the Weaving Process

In order to guarantee the formation of a high-quality loop during the rope drive operation, a sufficient time had to be provided for the formation of the loop. Therefore, a specific time sequence of the weaving operations, shown in Figure 4, needed to be designed to facilitate the completion of the entire weaving work. During weaving, first, the rope drive leads the loop to the established position S_0 during time t_0; then, in the time interval $t_0 \sim t_1$, the thread picking device reaches the position S_3 and loosens the weaving fiber. During the time interval $t_1 \sim t_3$, the rope drive remains stationary. Due to a phase difference of one-cycle between the thread picking operation and the hooking operation, the hooking needles move downward and upward to pick the loop, while the thread picking device moves upward and downward to loosen and tighten the weaving fiber. During the time interval $t_3 \sim t_4$, the weaving mechanism returns to the initial position.

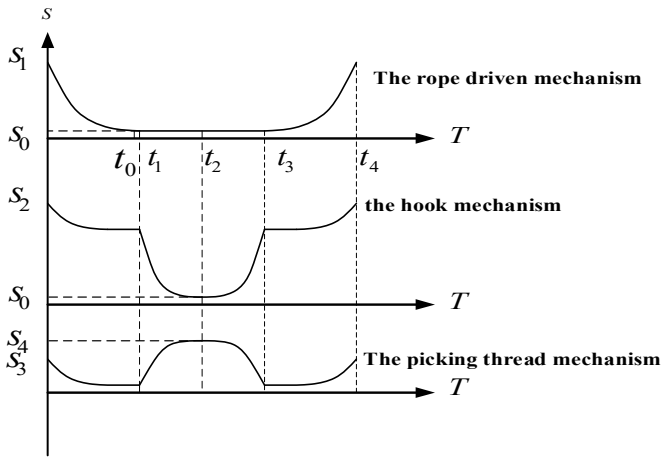


Figure 4. The time sequence diagram of the weaving mechanism [21].

Figure 5 shows the four steps of the weaving process.

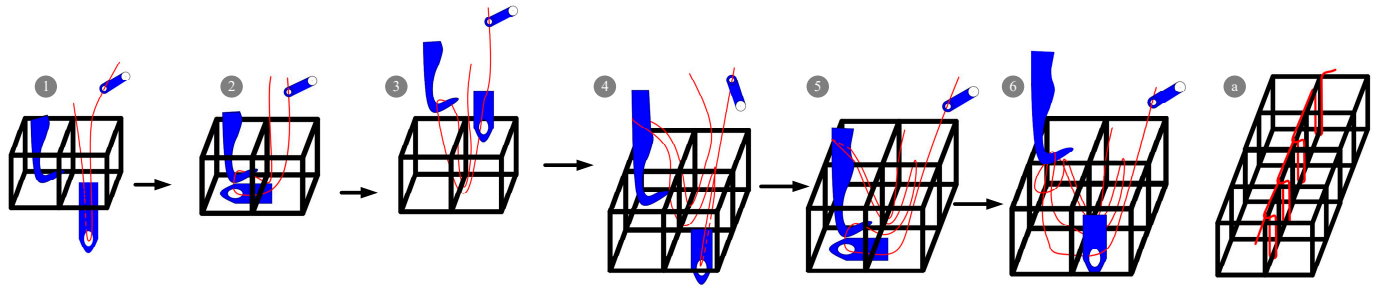


Figure 5. The weaving steps.

Step 1: The rope drive and hook mechanism move to the interior of the grid structure. It is necessary to maintain a suitable distance between the ends of the rope drive and the hook in the vertical direction for the convenience of the subsequent operation of hooking the loop.

Step 2: The motor controls the rotation of the reel to drive the operation of the rope, transmitting the lead head at the end of the rope drive to the bottom of the crochet needle, during which the hook remains stationary. Afterwards, the rope drive stops running, and the hook moves up and down. Due to the special structure of the crochet needle, the hook does not pick the loop during the downward process, while it picks it during the upward process.

Step 3: The thread picking device tightens the thread ring, and the rope drive motor runs in reverse to reset the lead head to the position in step 1. Then, the weaving system is raised above the grid.

Step 4: The weaving system carrying the thread ring is moved inside the next grid structure, during which the thread loop slides onto the crochet-connecting rod.

Step 5: The motions of the rope drive and hook remain consistent with those of in step 2.

Step 6: The new picked thread loop is introduced into the previous loop. The thread picking device tightens the thread to disengage the previous loop from the hook. These steps are repeated to complete the entire weaving process. The final weaving structure is shown in the step a in Figure 5.

4. Kinematic Analysis of the Rope Drive Mechanism

4.1. Forward Kinematic Analysis of the Mechanism

The motion of a rigid body in three-dimensional space R^3 can be defined as $g(p) = Rp + t$, where $t \in R^3$, $R \in SO(3)$. The entire mapping of the motion forms a six-dimensional Lie group [22–25], which is called a special Euclidean group, is indicated as $SE(3)$

$$SE(3) = (R, t), \tag{1}$$

where R represents the 3×3 attitude rotation matrix, t is the position vector.

According to Euler's theorem, there is always a rotation matrix corresponding to each rotational motion of a rigid body. Set the unit vectors ω representing the rotation axis and θ representing the rotation angle, then R can be determined as a function containing ω and θ:

$$R = e^{\theta\hat{\omega}} \tag{2}$$

where $\hat{\omega}$ is the antisymmetric matrix.

According to the mapping relationship of the index, it can be concluded that:

$$\begin{aligned} e^{\theta\hat{\omega}} &= E + \hat{\omega}sin\theta + \hat{\omega}^2(1 - cos\theta), \\ \hat{\xi} &= \begin{pmatrix} \hat{\omega} & v \\ 0 & 0 \end{pmatrix}_{4\times4} \in R^{4\times4} \\ \xi &= \begin{pmatrix} \hat{\omega} & v \\ 0 & 0 \end{pmatrix}^{\vee}_{4\times4} = \begin{pmatrix} \omega \\ v \end{pmatrix}_{6\times1} \end{aligned} \tag{3}$$

where $\hat{\xi}$ is the motion screw, ξ is the screw coordinates of $\hat{\xi}$.

Based on Chasles' theorem [26–29], any rigid body motion can be achieved through spiral motion, which is a composite motion containing the rotation around a certain axis and the movement along that axis. Therefore, a rigid body motion can be expressed as the exponential product of screw:

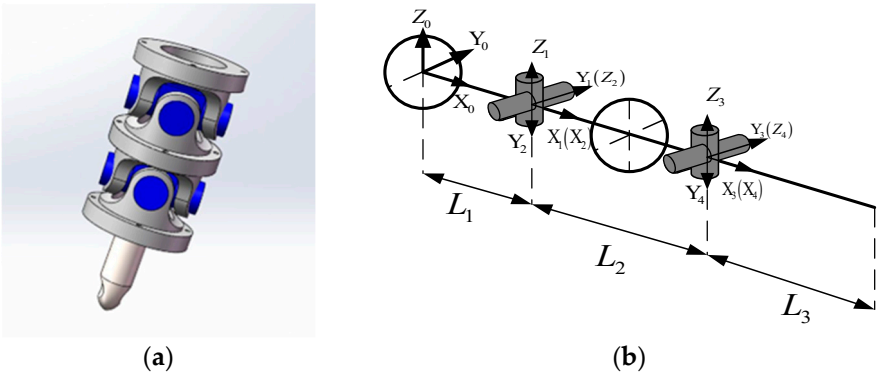
$$g = e^{\theta\hat{\xi}} = \begin{bmatrix} e^{\theta\hat{\omega}} & \left(E - e^{\theta\hat{\omega}}\right)(\omega \times v) + \theta\omega\omega^T v \\ 0 & 1 \end{bmatrix} \tag{4}$$

Therefore, the product of exponentials (POE) formula for the forward kinematics of serial robots is:

$$\begin{matrix} S \\ T \end{matrix}\mathcal{g}(\theta) = e^{\theta_1\hat{\xi}_1}e^{\theta_2\hat{\xi}_2}\cdots e^{\theta_n\hat{\xi}_n}\begin{matrix} S \\ T \end{matrix}\mathcal{g}(0) \tag{5}$$

According to the initial configuration and size of the rope drive shown in Figure 6, the unit vector of each joint axis direction can be derived as:

$$\begin{aligned} \omega_1 = \omega_3 &= \begin{bmatrix} 0 & 0 & 1 \end{bmatrix}^T, \ \omega_2 = \omega_4 = \begin{bmatrix} 0 & 1 & 0 \end{bmatrix}^T \\ r_1 = r_2 &= \begin{bmatrix} L_1 & 0 & 0 \end{bmatrix}^T, \ r_3 = r_4 = \begin{bmatrix} L_1 + L_2 & 0 & 0 \end{bmatrix}^T \end{aligned} \tag{6}$$



(**a**) (**b**)

Figure 6. (**a**) Three-dimensional diagram of the rope drive mechanism; (**b**) schematic diagram of the rope drive mechanism.

In the initial state, the pose matrix of the coordinate system T for the rope drive's end effectors, which is relative to the base coordinate system S, can be represented as:

$$ {}^{S}_{T}g(0) = \begin{bmatrix} 1 & 0 & 0 & L \\ 0 & 1 & 0 & 0 \\ 0 & 0 & 1 & 0 \\ 0 & 0 & 0 & 1 \end{bmatrix} \tag{7} $$

where $L = L_1 + L_2 + L_3$.

The forward kinematic solution of the rope drive mechanism is:

$$ {}^{S}_{T}g(\theta) = e^{\theta_1 \widehat{\xi}_1} e^{\theta_2 \widehat{\xi}_2} e^{\theta_3 \widehat{\xi}_3} e^{\theta_4 \widehat{\xi}_4} {}^{S}_{T}g(0) \tag{8} $$

According to designed dimensions of the rope drive, we obtain:

$$ L_1 = 0.6 \text{ mm}; L_2 = L_3 = 1.2 \text{ mm} ; \ L_4 = 1 \text{ mm} $$

The rope drive operation is driven by the rope, which can only be stretched but not compressed. Therefore, the structural design of the conduit should meet the controllable requirements of the conduit to ensure that the tension of the rope cannot exceed the rotation centerline of the joint, and, thereby, the system can rotate flexibly under the action of rope tightening and loosening, as shown in Figure 7.

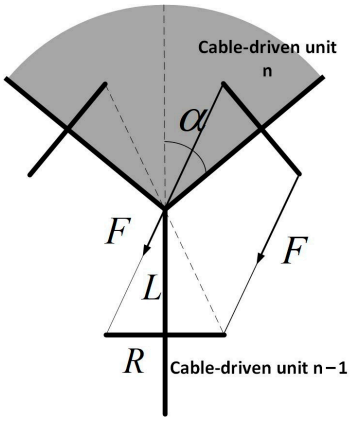


Figure 7. The limit position of the joint angle.

Consequently, to avoid entanglement during the rotation of the rope drive, the following requirements are necessary to be satisfied:

$$\theta \leq \alpha = 2\arctan\frac{R}{L} \tag{9}$$

where $R = 0.5$ mm, $L = 0.6$ mm, θ represents the rotation angle of the joints.

Then, $\theta \in (-0.44\pi, 0.44\pi)$.

According to the base coordinate system and the scope of the rotational angle of each joint, using the software Matlab2019 based on the Monte Carlo method [30], the operating space of the rope drive can be drawn, as shown in Figure 8.

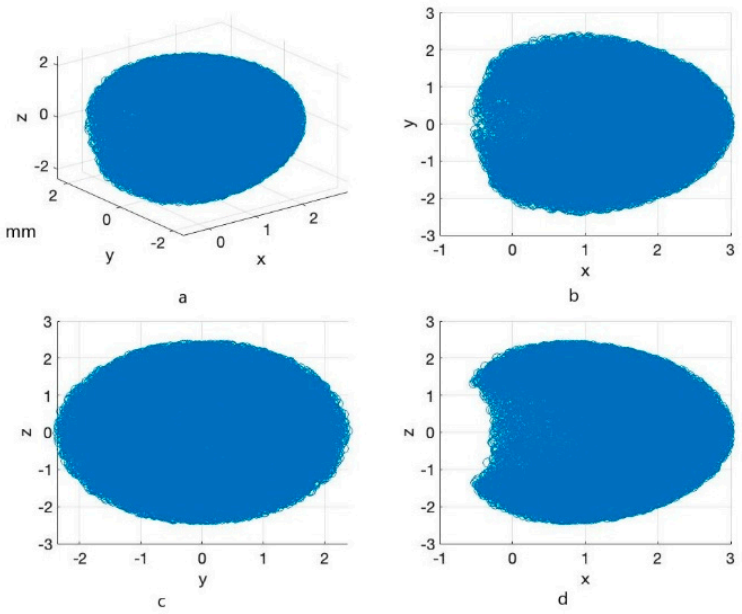


Figure 8. The operating space. (**a**) Three-dimensional diagram; (**b**) *XOY* planar projection; (**c**) *YOZ* planar projection; (**d**) *XOZ* planar projection.

4.2. Inverse Kinematics Analysis of the Rope Drive Mechanism

The inverse kinematics solution based on the theory of spinors is built on several basic subproblems, commonly referred to as the Paden–Kahan subproblems. The rope drive designed in this paper has four revolving shafts. The revolving shaft 1 and revolving shaft 2 are mutual orthogonal to the point q_1, the revolving shaft 3 and revolving shaft 4 are mutual orthogonal to the point q_2. In addition, the plane where the axis 1 and axis 2 are located is parallel to the plane where the revolving shaft 3 and revolving shaft 4 are located.

If a point lies on the axis of rotation, its coordinates remain unchanged, no matter how it rotates around the axis of rotation.

Hence, for the intersection point q_2:

$$\begin{gathered} q_2 = \begin{bmatrix} L_1 + L_2 & 0 & 0 \end{bmatrix}^T \\ e^{\theta_3 \widehat{\xi}_3} e^{\theta_4 \widehat{\xi}_4} q_2 = q_2 \end{gathered} \tag{10}$$

Set

$${}^S_T g(\theta) {}^S_T g(0)^{-1} = e^{\theta_1 \widehat{\xi}_1} e^{\theta_2 \widehat{\xi}_2} e^{\theta_3 \widehat{\xi}_3} e^{\theta_4 \widehat{\xi}_4} = g_1 \tag{11}$$

Then

$$q = e^{\theta_1 \widehat{\xi}_1} e^{\theta_2 \widehat{\xi}_2} e^{\theta_3 \widehat{\xi}_3} e^{\theta_4 \widehat{\xi}_4} q_2 = e^{\theta_1 \widehat{\xi}_1} e^{\theta_2 \widehat{\xi}_2} q_2 = g_1 q_2 = \begin{bmatrix} q_x & q_y & q_z \end{bmatrix}^T \tag{12}$$

Therefore, θ_2 can be calculated through the Paden–Kahan subproblem 2.

As shown in Figure 9, point $p = q_2 = \begin{pmatrix} L_1 + L_2 & 0 & 0 \end{pmatrix}$ rotates by the angle θ_2 around the axis ξ_2 to point p_1; then, point p_1 rotates by the angle θ_1 around the axis ξ_1 to point p.

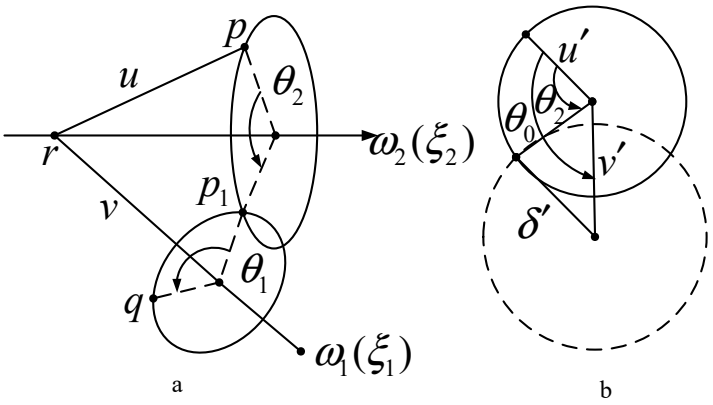


Figure 9. (**a**) The spiral motion of joints 1 and 2; (**b**) projection of the spiral motion.

Take a point t_1 located on the axis ξ_1 and a point t_2 located on the axis ξ_2.

$$t_1 = \begin{bmatrix} L_1 & 0 & 1 \end{bmatrix} t_2 = \begin{bmatrix} L_1 & 1 & 0 \end{bmatrix} \tag{13}$$

Based on the principle of keeping distance constant:

$$\left\| e^{\theta_2 \widehat{\xi}_2} p - t_1 \right\| = \|q - t_1\| \tag{14}$$

Then, define

$$\begin{gathered} \delta = \|q - t_1\|, u = p - t_2, v = t_1 - t_2 \\ u' = u - \omega_2 {\omega_2}^T u, v' = v - \omega_2 {\omega_2}^T v, {\delta'}^2 = \delta^2 - \left\| {\omega_2}^T (p - t_1) \right\| \end{gathered} \tag{15}$$

where u', v', and δ' are the projections of u, v and δ on the plane perpendicular to the axis ξ_2

$$\begin{gathered} \theta_0 = a \tan 2(\omega_2^T (u' \times v'), {u'}^T v') \\ \theta_2 = \theta_0 \pm ar \cos\left(\frac{\|u'\|^2 + \|v'\|^2 - \delta^2}{2\|u'\|\|v'\|}\right) \end{gathered} \tag{16}$$

where θ_0 is the angle between vectors u' and v'

$$\begin{gathered} u = \begin{bmatrix} q_x - L_1 & q_y & q_z - 1 \end{bmatrix}^T \\ v = \begin{bmatrix} 0 & -1 & 1 \end{bmatrix}^T \\ \omega_2 = \begin{bmatrix} 0 & 1 & 0 \end{bmatrix}^T \end{gathered} \tag{17}$$

Having determined the angle θ_2, θ_1 can be calculated through the Paden–Kahan subproblem 1, as shown in Figure 10.

$$\begin{gathered} p_1 = e^{\theta_2 \widehat{\xi}_2} p = \begin{bmatrix} p_x & p_y & p_z \end{bmatrix} \\ e^{\theta_1 \widehat{\xi}_1} q_2 = p_1 \end{gathered} \tag{18}$$

Then

$$\begin{gathered} u = p_1 - r = \begin{bmatrix} p_x - L_1 & p_y & p_z \end{bmatrix} \\ v = q - r = \begin{bmatrix} L_2 & 0 & 0 \end{bmatrix}^T \\ \omega_1 = \begin{bmatrix} 0 & 0 & 1 \end{bmatrix}^T \end{gathered} \tag{19}$$

where

$$u' = u - \omega_1{\omega_1}^T u, v' = v - \omega_1{\omega_1}^T v$$
$$\theta_1 = a\tan 2(\omega_1^T(u' \times v'), {u'}^T v') \tag{20}$$

Having determined θ_1 and θ_2, θ_3 and θ_4 can also be calculated through the above-mentioned method.

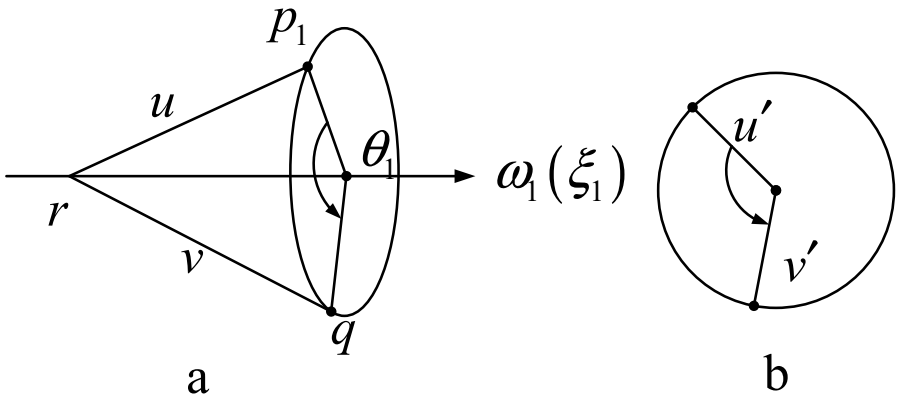


Figure 10. (**a**) The spiral motion of joint 1; (**b**) projection of the spiral motion.

5. Results and Discussion

Based on the layout and size chain relationship of the drafting mechanism, the position coordinates of the end of the hook needle in the coordinate system of the rope drive could be obtained as $\begin{bmatrix}1.6\text{ mm} & 1.2\text{ mm} & -1.6\text{ mm}\end{bmatrix}$.

Then, the inverse kinematics solution algorithm provided was used to obtain the rotation angles of each joint of the rope drive at this position. Four sets of solutions, shown in Table 1, were obtained.

Table 1. The calculated rotation angles of the joints.

θ_1	(Degree)	θ_2	θ_3	θ_4
29.978812		29.998971	30.013216	29.987864
209.988781		−209.987698	30.013216	29.987864
29.978812		29.998971	−149.889769	−209.99878
209.988781		−209.987698	−149.889769	−209.99878

According to the rotation angle calculated earlier, only one set of solutions satisfied the requirements. We substituted this set of solutions into the forward kinematics solution equation to obtain the end pose of the rope drive.

$$\theta_1 = \quad 29.978812 \quad \theta_2 = 29.998971 \quad \theta_3 = 30.013216 \quad \theta_4 = 29.987864$$
$${}^S_T\mathcal{g}(\theta) = e^{\theta_1\widehat{\xi}_1}e^{\theta_2\widehat{\xi}_2}e^{\theta_3\widehat{\xi}_3}e^{\theta_4\widehat{\xi}_4}{}^S_T\mathcal{g}(0) = \begin{bmatrix} 0.129487 & -0.808012 & 0.574759 & 1.625538 \\ 0.574759 & 0.533493 & 0.620512 & 1.209326 \\ -0.808012 & 0.250000 & 0.533493 & -1.616612 \\ 0.000000 & 0.000000 & 0.000000 & 1.000000 \end{bmatrix} \tag{21}$$

By comparison, the calculated data and the end coordinates were basically consistent. Therefore, it can be concluded that the forward and inverse kinematics analysis algorithm based on screw theory proposed in this paper has good numerical stability and accuracy. At the same time, the results also verified that the weaving mechanism designed in this study could complete the basic steps of weaving.

For the dynamic simulation analysis of the weaving mechanism, three-dimensional models of the rope drive and the hook were established and then imported into the software Adams. The specific simulation steps were as follows: first, the constrains of each part were

defined based on the designed weaving mechanism; second, the drive for each joint was set, and the direction of movement was adjusted properly; third, the calculated motion parameters for the weaving mechanism derived from forward and inverse kinematics were imported to the editor of Adams; fourth, we set the points at the end of the lead system and the hook as the target, then started the drive to obtain the trajectory coordinates of the target points. Last, the trajectory coordinates were processed through software Matlab2019 to draw a three-dimensional map of the trajectory, as shown in Figure 11. The red line and blue line represent the end trajectories of the lead system and the hook, respectively. The lead system runs from the initial position A to position B, and the hook runs from the initial position C to position B. The trajectories converge at point B to complete the hook work, which verified the accuracy of the forward and inverse solutions calculated through screw theory. In addition, the dynamic simulation also indicated the rationality and feasibility of the designed weaving mechanism in small, enhanced grids.

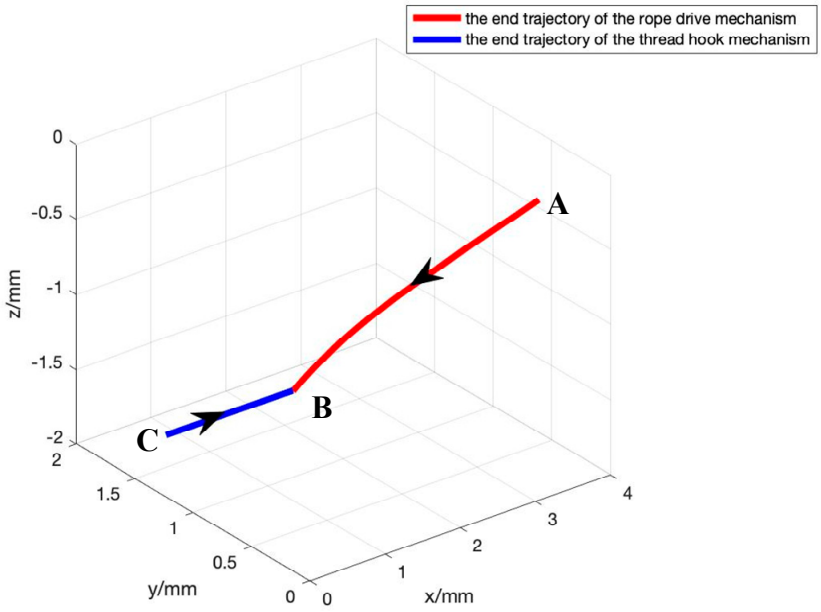


Figure 11. The trajectory of the weaving mechanism. (A) the initial position of the end of the rope drive mechanism; (B) the intersection position; (C) the initial position of the end of the thread hook mechanism.

Through trajectory simulation analysis of the model, the coordinates of the intersection point B located in the trajectory of the weaving mechanism could be obtained as $[1.60928\ \text{mm} \quad 1.21097\ \text{mm} \quad -1.59492\ \text{mm}]$ and were basically consistent with the calculated results of forward and inverse kinematics. By comparing the results of the theoretical calculations with those of the trajectory simulation analysis, we proved that the designed weaving mechanism could complete the weaving operation in a small 4 mm × 4 mm × 4 mm space. However, a limitation is that we have not produced a prototype for experimental testing, which is the focus of our future work.

6. Conclusions

In order to achieve personalized weaving operations in small-sized spaces, this paper proposes a new composite forming technology and weaving mechanism based on grid-enhanced structures. First, we combined the 3D printing technology, the continuous fiber printing technology and the weaving technology to formulate a specific weaving process principle. Second, we completed the design and modeling of the weaving mechanism. In addition, we analyzed the design's logic, the motion timing and the specific weaving steps of each element in the weaving system. Third, we analyzed the forward and inverse kinematics of the rope drive based on screw theory and drew the operating space. Finally,

based on the end position of the hook, the rotation angle of each joint was calculated, and the calculated results were verified by forward kinematics analysis. We also conducted a dynamic simulation analysis of the weaving mechanism through Adams software. The simulated trajectories converged successfully to complete the hook work, which further verified the accuracy of the forward and inverse solutions obtained according to screw theory. Moreover, the dynamic simulation also indicated the rationality and feasibility of the designed weaving mechanism in small, enhanced grids.

In the future, we will produce a prototype based on the designed weaving mechanism and conduct experiments to obtain weaving trajectory, weaving space and weaving dimensional accuracy to verify the simulation results.

Author Contributions: Conceptualization, J.W. and W.Z.; methodology, J.W. and W.Z.; software, J.W.; validation, J.W. and W.Z.; formal analysis, J.W.; investigation, J.W.; resources, J.W.; data curation, W.Z.; writing—original draft preparation, J.W.; writing—review and editing, J.W.; visualization, J.W.; supervision, W.Z. All authors have read and agreed to the published version of the manuscript.

Funding: This research received no external funding.

Institutional Review Board Statement: Not applicable.

Informed Consent Statement: Not applicable.

Data Availability Statement: Not applicable.

Conflicts of Interest: The authors declare no conflict of interest.

References

1. Li, X.P.; He, X.H.; Liang, J.H.; Song, Y.F. Research Status of 3D Braiding Technology. *Appl. Compos. Mater.* **2022**, *29*, 147–157.
2. Chen, X.; Taylor, L.W.; Tsai, L.J. Three-dimensional fabric structures. Part 1—An overview on fabrication of three-dimensional woven textile preforms for composites sciencedirect. In *Handbook of Technical Textiles*, 2nd ed.; Woodhead Publishing: Cambridge, UK, 2016; pp. 285–304.
3. Bilisik, K. Three-dimensional braiding for composites: A review. *Text. Res. J.* **2013**, *83*, 1414–1436. [CrossRef]
4. Gries, T.; Bettermann, I.; Blaurock, C.; Bundgens, A.; Dittel, G.; Emonts, C. Aachen Technology Overview of 3D Textile Materials and Recent Innovation and Applications. *Appl. Compos. Mater.* **2022**, *29*, 43–64. [CrossRef]
5. Gloy, Y.S.; Neumann, F.; Wendland, B.; Stypa, O.; Gries, T. Overview of developments in technology and machinery for the manufacture of 3D-woven fabrics. In Proceedings of the Third World Conference on 3D Fabrics and Their Applications, Wuhan, China, 20–21 April 2011; pp. 57–62.
6. Zhang, D.; Sun, Y.; Wang, X.; Chen, L. Prediction of macro-mechanical properties of 3D braided composites based on fiber embedded matrix method. *Compos. Struct.* **2015**, *134*, 393–408.
7. Lu, Z.; Xia, B.; Yang, Z. Investigation on the tensile properties of three-dimensional full five directional braided composites. *Comput. Mater. Sci.* **2013**, *77*, 445–455. [CrossRef]
8. Hu, L.; Tao, G.; Liu, Z. Investigation on the Yarn Squeezing Efect of Three Dime-nsional Full Five Directional Braided Composites. *Appl. Compos. Mater.* **2019**, *26*, 371–387.
9. Ko, F.; Theelen, K.; Amalric, E. 3D braiding technology: A historical prospective. In Proceedings of the Third World Conference on 3D Fabrics and Their Applications, Wuhan, China, 20–21 April 2011.
10. Liu, Q.; Li, J.; Li, X. Influence of 3D Braiding Technology Parameters on Tensile Properties of Composites. *Aerosp. Mater. Technol.* **2000**, *30*, 55–58.
11. Schreiber, F.; Theelen, K.; Südhoff, E.S.; Lee, H.Y.; Ko, F.K.; Gries, T. 3D-hexagonal braiding possibilities in near-net shape preform production for lightweight and medical applications. In Proceedings of the 18th International Conference on Composite Materials, Jeju Island, Republic of Korea, 21–26 August 2011.
12. Tolosana, N.; Lomov, S.V.; Miravete, A. Development of a Simulation Tool for 3D Braiding Architectures. *AIP Conf. Proc.* **2007**, *907*, 1005–1010.
13. Gao, Y.T.; Ko, F.K.; Hu, H. Integrated Design for Manufacturing of Braided Preforms for Advanced Composites Part II: 3D Braiding. *Appl. Compos. Mater.* **2013**, *20*, 1065–1075. [CrossRef]
14. Tang, X.Q. An Overview of the Development for Cable-Driven Parallel Manipulator. *Adv. Mech. Eng.* **2014**, *6*, 823028. [CrossRef]
15. Deng, Y.P.; Bai, L.; Long, Z.; Guan, J.; Chen, X.H.; Hou, J.Z.; Duan, W.B. Research on Cable-driven Robots. In Proceedings of the 2018 International Conference on Advanced Control, Automation and Artificial Intelligence, Shenzhen, China, 21–22 January 2018; Volume 155, pp. 41–47.
16. Khomami, A.M.; Najafi, F. A survey on soft lower limb cable-driven wearable robots without rigid links and joints. *Robot. Auton. Syst.* **2021**, *144*, 103846. [CrossRef]

17. Haga, Y.; Tanahashi, Y.; Esashi, M. Small Diameter Active Catheter Using Shape Memory Alloy. In Proceedings of the MEMS 98. IEEE. Eleventh Annual International Workshop on Micro Electro Mechanical Systems. An Investigation of Micro Structures, Sensors, Actuators, Heidelberg, Germany, 25–29 January 1998; pp. 419–424.
18. Haga, Y.; Muyari, Y.; Mineta, T. Small diameter hydraulic active bending catheter using laser processed super elastic alloy and silicone rubber tube. In Proceedings of the 2005 3rd IEEE/EMBS Special Topic Conference on Microtechnology in Medicine and Biology, Oahu, HI, USA, 12–15 May 2005.
19. Chang, J.K.; Chung, S.; Lee, Y.; Park, J.; Lee, S.K. Development of endovascular microtools. *J. Micromech. Microeng.* **2002**, *12*, 824–831. [CrossRef]
20. Cimino, W.W. *Active Tip Control for Small Diameter Catheters: Power Transmission and Transduction Requirements*; The University of Utah: Salt Lake City, UT, USA, 1992.
21. Wei, J.K.; Hab, W.P.; Zhang, W.X.; Ding, X.L. The design and analysis of 3D braiding mechanism based on a small-size additive manufacturing technology reinforced by continuous fiber. In Proceedings of the IFToMM China International Conference on Mechanism and Machine Science & Engineering, Yantai, China, 30 July–1 August 2022.
22. Liu, W.F.; Gong, Z.B.; Wang, Q.Q. Investigation on Kane dynamic equations based on screw theory for open-chain manipulators. *Appl. Math. Mech. Engl. Ed.* **2005**, *26*, 627–635.
23. Karakus, S.O. Screw Theory in Lorentzian Space. *Adv. Appl. Clifford Algebras* **2019**, *29*, 1. [CrossRef]
24. Lipkin, H.; Duffy, J. Sir Robert Stawell Ball and methodologies of modern screw theory. *Proc. Inst. Mech. Eng. Part C J. Mech. Eng. Sci.* **2002**, *216*, 1–11. [CrossRef]
25. Yu, H.; Li, B.; Yang, X.; Hu, Y. Structural synthesis and variation analysis of a family of 6-dof parallel mechanisms with three limbs. *Int. J. Robot. Autom.* **2010**, *25*, 121–131. [CrossRef]
26. Zhu, D.C.; Xiao, F.; Wang, L.; Gu, Q.H. Configuration Design and Kinematic Analysis on Some New 2R1T 3-DOF Parallel Robots. *Key Eng. Mater.* **2011**, *474–476*, 840–845. [CrossRef]
27. Lee, U.K.; Han, C.S. A method for predicting dynamic behaviour characteristics of a vehicle using the screw theory—Part I. *Proc. Inst. Mech. Eng. Part D J. Automob. Eng.* **2008**, *222*, 65–67. [CrossRef]
28. Sariyildiz, E.; Temeltas, H. Solution of Inverse Kinematic Problem for Serial Robot Using Quaterninons. In Proceedings of the 2009 IEEE International Conference on Mechatronics and Automation, Changchun, China, 9–12 August 2009; pp. 26–31.
29. Wang, J.; Gosselin, C.M.; Huang, Z. Analysis of the kinematic characteristics of 3 DOF mechanisms. In Proceedings of the Eleventh World Congress in Mechanism and Machine Science, Tianjin, China, 1–4 April 2004; pp. 153–157.
30. Cunha, A.; Nasser, R.; Sampaio, R. Uncertainty quantification through the Monte Carlo method in a cloud computing setting. *Comput. Phys. Commun.* **2014**, *185*, 1355–1363. [CrossRef]

Disclaimer/Publisher's Note: The statements, opinions and data contained in all publications are solely those of the individual author(s) and contributor(s) and not of MDPI and/or the editor(s). MDPI and/or the editor(s) disclaim responsibility for any injury to people or property resulting from any ideas, methods, instructions or products referred to in the content.